Enhancing a Convolutional Autoencoder with a Quantum Approximate Optimization Algorithm for Image Noise Reduction

Tara Kit¹, Kimsay Pov¹, Kimleang Kea¹, Won-Du Chang¹, Hee Chul Park², and Youngsun Han^{1,*}

- ¹ Department of AI Convergence, Pukyong National University, Busan 48513, South Korea
- ² Department of Physics, Pukyong National University, Busan 48513, South Korea
- * Authors to whom any correspondence should be addressed.

E-mail: youngsun@pknu.ac.kr

Abstract. Image denoising is essential for removing noise in images caused by electric device malfunctions or other factors during image acquisition. It ensures the preservation of image quality and accurate interpretation. Many convolutional autoencoder algorithms have proven effective in image denoising. Owing to their promising efficiency, quantum computers have gained popularity. This paper proposes a method, the quantum convolutional autoencoder (QCAE), which enhances traditional convolutional autoencoders by replacing their latent space with a quantum counterpart implemented via a QAOA-inspired ansatz circuit. To enhance efficiency, we leveraged the advantages of the quantum approximate optimization algorithm (QAOA)-incorporated parameter-shift rule to identify an optimized cost function, facilitating effective learning from data and gradient computation on an actual quantum computer. The proposed QCAE method outperformed its classical counterpart as it exhibited lower training loss and a higher structural similarity index (SSIM) value. QCAE also outperformed its classical counterpart in denoising the MNIST dataset by up to 40% in terms of SSIM value, confirming its enhanced capabilities in real-world applications. Evaluation of QAOA performance across different circuit configurations and layer variations showed that our technique outperformed other circuit designs by 25\% on average.

Keywords: Quantum computing, Quantum convolutional autoencoder, Variational quantum algorithm, Quantum machine learning

Submitted to: Mach. Learn.: Sci.

1. Introduction

Images acquired from image sensors frequently exhibit noise caused by hardware malfunctions and various environmental factors. In this context, noise denotes unpredictable fluctuations in brightness, intensity, or color information within a digital image [1, 2]. Image denoising is pivotal for eliminating these distortions from a given input image, aiming to generate a more refined and clearer image [3, 4]. The denoising process is essential for accurate image analysis and benefits both human interpretation and machine learning (ML)-based assessments [5].

An autoencoder (AE) is an unsupervised neural network model designed for reconstructing its input through a learned latent representation. This class of models demonstrates notable versatility, particularly in the group of learning representations [6]. AEs encompass numerous successful variants, including the variational autoencoder (VAE), convolutional autoencoder (CAE), and denoising autoencoder, as discussed in [7]. They operate by mapping the input to a lower-dimensional space (latent space). These encoding and decoding steps are subsequently used to accurately reconstruct the original image. However, the latent space in AE encounters challenges in accurately capturing complex, nonlinear relationships among data points. Moreover, it often prioritizes frequent data patterns, resulting in sparse or poorly structured latent representations that underrepresent rare samples. This can reduce effectiveness in generative or reconstruction tasks [8].

Recently, the popularity of quantum computers has surged among researchers, driven by their unique computational capabilities, such as superposition. Quantum circuits leverage principles such as superposition, entanglement, and interference, allowing them to represent and manipulate complex, high-dimensional states that are often intractable for classical systems. This capability can lead to more accurate and efficient data compression than classical AE. However, quantum computers remain suboptimal for production applications [9]. The existing quantum computing (QC) landscape is in the noisy intermediate-scale quantum (NISQ) era [10], indicating that current quantum systems exhibit limitations in terms of the number of qubits, circuit depth, and high noise levels. Because of these factors, variational quantum algorithms (VQAs) have emerged as an ideal choice for implementation, primarily due to their lower qubit requirements and reduced circuit depth. VQAs leverage classical computation to optimize the algorithm parameters effectively [11]. In addition, they exhibit robustness against image noise - a major problem for other types of quantum algorithms. We adopt a QAOA-inspired ansatz circuit, leveraging its parameterized structure to construct a quantum latent space representation, rather than applying QAOA for solving an optimization task. These quantum principles, superposition, entanglement, and interference, allow the circuit to represent and process complex, high-dimensional patterns in data. In our approach, this variational structure enables effective learning and denoising of noisy images through gradient-based optimization, rather than through solving a combinatorial objective.

Due to exponentially increasing computational power and the ability to learn data representations in higher-dimensional spaces, our primary objective in this study is to integrate CAE and QAOA to create an advanced latent space for execution within QC. We enhanced our model by incorporating a trainable quantum variational circuit to develop a hybrid architecture termed a quantum convolutional autoencoder (QCAE). The QCAE was specifically designed for the task of MNIST [12] image denoising. To showcase its efficacy, we conducted a comparative analysis of its performance against its classical counterpart, the classical convolutional autoencoder (CCAE). The contributions of this study are as follows:

- We present an approach where the convolutional autoencoder ensures efficient feature extraction, while the QAOA-inspired ansatz circuit contributes the advantage of reduced qubit requirements and improved suitability for NISQ devices.
- We leverage a QAOA-inspired ansatz circuit to replace the classical latent space, enabling the representation of input data in a higher-dimensional quantum space for improved feature extraction and denoising.
- We apply the parameter-shift rule (PSR) to efficiently and precisely compute gradients of the QAOA-inspired ansatz circuit, enabling stable optimization within hybrid quantum-classical training.
- We rigorously conducted denoising experiments using the MNIST dataset, exploring diverse image noise (Gaussian noise) factors across both quantum simulation and machine scenarios.

The rest of the paper is organized as follows. Section 2 describes both classical and quantum algorithms for image denoising and classification. Section 3 reviews the associated background to understand this paper. In Section 4, we delve into the details of our proposed methodology, leveraging QAOA in conjunction with PSR optimization. Section 5 details the specifics of the dataset and environments employed in our study. In Section 6, we present a comprehensive showcase of our superior performance in image denoising. Finally, Section 7 concludes the paper.

2. Related works

In the field of classical image denoising, deep learning serves as the main building block, harnessing the power of neural networks (NN) to effectively reduce noise and enhance image quality.

In the field of classical image denoising, deep learning serves as the main building block, harnessing the power of neural networks to effectively reduce noise and enhance image quality [3, 4]. Autoencoders and their variants, including convolutional autoencoders, have been widely applied to natural images and benchmark datasets, demonstrating strong denoising performance [13]. These methods form the baseline context against which hybrid quantum–classical approaches, such as our QCAE, can be evaluated.

Numerous studies leverage QC and NN to develop image classification and denoising. Bravo et al. [14] presented an enhanced feature quantum autoencoder, a VQA capable of compressing the quantum states of different models with higher fidelity. They validated the method in simulations by compressing the ground states of the Ising model and classical MNIST handwritten digits. Although this approach effectively compressed and reconstructed images, its primary design did not prioritize the task of denoising images. Rivas et al. [15] presented a hybrid QML approach for representation learning. They utilized a quantum variational circuit that could be trained using conventional gradient descent techniques. To further enhance its performance, the method dressed the quantum circuit with AE layers for meaningful interpretation of complex unstructured data. Orduz et al. [16] applied randomized quantum circuits to process input data, functioning as quantum convolutions to generate representations applicable in convolutional networks. The experimental findings indicate comparable performance to traditional convolutional neural networks, with quantum convolutions demonstrating potential acceleration in convergence in certain scenarios. Nguyen et al. [17] used a D-Wave 2X quantum computer to address NP-hard sparse coding problems in image classification. The method involves downsampling MNIST images, employing a bottleneck autoencoder, and using quantum inference on D-Wave 2X to obtain sparse binary representations. The study also explored lateral inhibition between features generated from a subset of autoencoder-reduced MNIST images. Sleeman et al. [18] proposed a hybrid system that integrates a classical AE with a quantum annealing restricted Boltzmann machine (RBM) on a D-Wave quantum computer. The system achieved a nearly 22-fold compression of grayscale images to binary with lossy recovery. The evaluation of the MNIST dataset demonstrated the feasibility of using D-Wave as a sampler for ML. Additionally, the study compared the results of a hybrid quantum RBM with a hybrid classical RBM in a downstream classification problem and measured image similarity between MNIST-generated images and the original training dataset.

3. Preliminaries

In this section, we introduce the basics of QC and its data processing. We then explore how quantum computers handle classical data, discuss the execution of parameterized circuit data, and present the foundation of CCAE as our proposed method counterpart.

3.1. Quantum computing (QC)

Quantum computing leverages fundamental principles such as superposition, entanglement, and quantum interference to explore new computational paradigms, with the potential for advantages in specific tasks over classical systems [19].

3.1.1. Quantum bit (Qubit) The operational architecture of quantum computers differs fundamentally from that of classical computers. Quantum computers use quantum bits

(qubits) as operational units, unlike classical computers, which rely on binary digits existing in either state 0 or 1. A qubit can exist simultaneously in a superposition of states 0, 1, and a linear combination of both 0 and 1 [20]. The basis states of $|0\rangle$ and $|1\rangle$ represent the computational basis states of a qubit, forming an orthonormal basis in a two-dimensional Hilbert space. Any pure qubit state can be expressed as a linear combination of these basis states, defined as follows:

$$|0\rangle = \begin{bmatrix} 1\\0 \end{bmatrix}, \quad |1\rangle = \begin{bmatrix} 0\\1 \end{bmatrix}, \quad |\psi\rangle = \alpha |0\rangle + \beta |1\rangle = \begin{bmatrix} \alpha\\\beta \end{bmatrix}.$$
 (1)

where the probability coefficients α and β are called *amplitudes*. The sum of the squared amplitudes in a superposition equals 1, which is $|\alpha|^2 + |\beta|^2 = 1$. Despite the ability of qubits to exist simultaneously in both $|0\rangle$ and $|1\rangle$ states, their definitive output is determined as either $|0\rangle$ or $|1\rangle$ when measured.

3.1.2. Quantum data manipulation Data on a qubit can be transformed and manipulated using quantum gates. These quantum gates fundamentally involve the modification of one or more qubits [21]. The gates introduced in this paper include Hardamard (H), CNOT, and rotation gates such as X-rotation (R_X) , Y-rotation (R_Y) , and Z-rotation (R_Z) . They are defined as follows:

$$H = \frac{1}{\sqrt{2}} \begin{bmatrix} 1 & 1 \\ 1 & -1 \end{bmatrix}, \quad \text{CNOT} = \begin{bmatrix} 1 & 0 & 0 & 0 \\ 0 & 1 & 0 & 0 \\ 0 & 0 & 0 & 1 \\ 0 & 0 & 1 & 0 \end{bmatrix}.$$
 (2)

$$R_X(\theta) = \begin{bmatrix} \cos\left(\frac{\theta}{2}\right) & -i\sin\left(\frac{\theta}{2}\right) \\ -i\sin\left(\frac{\theta}{2}\right) & \cos\left(\frac{\theta}{2}\right) \end{bmatrix}. \tag{3}$$

$$R_Y(\theta) = \begin{bmatrix} \cos\left(\frac{\theta}{2}\right) & -\sin\left(\frac{\theta}{2}\right) \\ \sin\left(\frac{\theta}{2}\right) & \cos\left(\frac{\theta}{2}\right) \end{bmatrix}. \tag{4}$$

$$R_Z(\theta) = \begin{bmatrix} e^{-i\theta/2} & 0\\ 0 & e^{i\theta/2} \end{bmatrix}. \tag{5}$$

All gates except CNOT are single-qubit gates. The H gate enables the creation of a superposition for a single qubit, while rotation gates allow a qubit to be positioned at any point on a Bloch sphere surface. However, CNOT is a two-qubit gate that facilitates entanglement between two qubits. These gates collectively enable quantum state manipulation.

3.2. Classical data encoding

Numerous QML algorithms require converting classical data into quantum states within quantum computers, a process known as data encoding [22, 23]. In other words, the dataset is initially translated from the subject data domain D to the Hilbert space H through a designated feature mapping process $f:D\to H$. One of the encoding techniques, specifically angle encoding or qubit encoding, is widely renowned for its ability to leverage a minimal number of qubits that correspond to the size of the input vector [24]. The angle encoding scheme demonstrates remarkable efficiency as it necessitates the rotation of only a single qubit, as depicted in Fig. 1.

$$|0\rangle - H - R_Y(\theta) - R_Z(\phi) - |\psi\rangle$$

Figure 1: Angle encoding quantum circuit.

In this technique, each data value x undergoes an initial normalization process, mapping it to the range $[0, 2\pi]$. Subsequently, it is encoded using single-qubit rotation gates R_X , R_Y , and R_Z . These rotation gates dynamically determine the rotation angle θ based on the corresponding data value x. The predominant technique involves applying the feature map $x \to cos\left(\frac{x}{2}\right)|0\rangle + sin\left(\frac{x}{2}\right)|1\rangle$ using the R_Y as follows:

$$R_{Y}(x) |0\rangle = \begin{bmatrix} \cos\left(\frac{x}{2}\right) & -\sin\left(\frac{x}{2}\right) \\ \sin\left(\frac{x}{2}\right) & \cos\left(\frac{x}{2}\right) \end{bmatrix} \begin{bmatrix} 1 \\ 0 \end{bmatrix}$$
$$= \cos\left(\frac{x}{2}\right) |0\rangle + \sin\left(\frac{x}{2}\right) |1\rangle.$$
(6)

As such, this approach requires n qubits to encode n input variables defined as follows:

$$|\psi_x\rangle = \bigotimes_{i=1}^n R(x_i)|\psi_0\rangle,\tag{7}$$

where R is one of the rotation gates and ψ_0 is an initial state.

3.3. Parameterized quantum circuit (PQC)

A PQC provides a practical framework for implementing variational algorithms on NISQ devices, enabling hybrid quantum-classical computations with limited qubits and circuit depth [25, 26]. Conceptually similar to a classical NN, it features trainable parameters within circuits comprising fixed gates, such as CNOT, and adjustable gates like rotation gates. It typically requires a low number of qubits and circuit depth. However, even with a limited number of qubits and circuit depth, certain classes of PQCs exhibit the ability to generate highly non-trivial outputs. Similar to classical NN, a higher circuit depth repeated in a PQC provides increased flexibility to the circuit, leading to superior results in various applications.

Consider a trainable unitary U_{θ} operating on an n-qubit state applied to a reference state $|\phi\rangle$, where the trained variable $|\phi_{\theta}\rangle = U_{\theta}|\phi\rangle$ generally equals to $|0\rangle^{\otimes n}$. Nevertheless, in the context of an n-qubit encoding, which represents a $2^n \times 2^n$ unitary mapping, the number of input qubits equals the number of output qubits. For the 8-qubit circuit, we encounter a total of $2^{16} = 65,536$ parameters, which proves to be an excessively high number for efficient optimization. Therefore, to enhance efficiency, we constrained gate shapes to have fewer parameters using small, efficient gates such as single-qubit rotations and entangling gates like CNOT as the fundamental building blocks of the overall unitary operation.

3.4. Classical convolutional autoencoder (CCAE)

An autoencoder (AE) is an unsupervised NN comprising an encoder E and a decoder D, coined in the 1980s [27]. It reconstructs input image data within its hidden layers, using the input as the expected output. The CCAE enhances this by substituting fully connected layers with convolutional layers, optimizing it for spatial data tasks, and ensuring superior feature extraction and representation learning. Like a typical AE, the CCAE maintains input and output layer sizes but transforms the decoder with transposed convolutional layers for enhanced decoding capabilities [28]. Fig. 2 illustrates the architecture of the CCAE, showcasing the process of deconstructing and reconstructing input image data. Through this transformation, the encoded data traverses the latent space Z, enabling the model to learn and focus specifically on crucial components of the input image data.

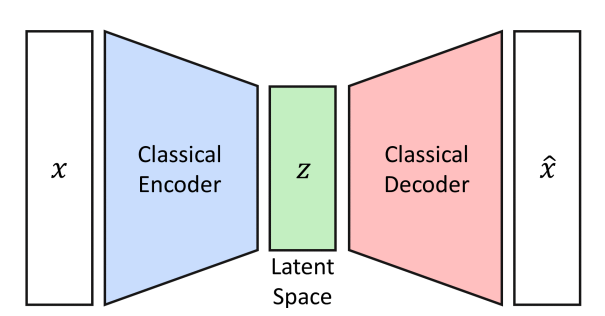


Figure 2: Architecture of classical convolutional autoencoder: The core design of a convolutional autoencoder consists of classical encoder and decoder components, each featuring crucial convolutional layers. These layers play a pivotal role in transforming the input image data x into a reconstructed representation \hat{X} through the latent space Z.

Given an input image data x, the process of CCAE is defined as follows:

$$\hat{x} = D(Z), Z = E(x), \tag{8}$$

the most commonly used training loss for autoencoders is the L2 reconstruction loss, defined as:

$$L_{AE} = \|x - \hat{x}\|^2,\tag{9}$$

and $\|\cdot\|^2$ denotes the L2-norm.

4. The proposed method

In this section, we present a comprehensive end-to-end methodology outlining the proposed approach. We first extensively review the proposed technique in its quantum form, after which we meticulously present the quantum circuit using the QAOA method. Finally, we explain how we fine tune and improve the quantum circuit through a training optimization process, focusing on a PSR technique.

4.1. Quantum convolutional autoencoder (QCAE)

In this study, we introduce the QCAE architecture designed for image denoising. Leveraging the CCAE model as its foundation, the QCAE incorporates a QAOA circuit to replace the CCAE's latent space. The QCAE process involves several key stages: i) pre-processing the input image data, which includes normalizing pixel values to the [0, 1] range, ii) introducing Gaussian noise to the input image data to generate a noisy input, iii) transforming the noisy input through classical convolutional layers to produce a latent representation, which is then encoded into a quantum state, iv) using a QAOA circuit to manipulate the quantum-encoded latent vector, v) measuring the output of the QAOA circuit, and vi) generating denoised input image data through a classical decoder based on the QAOA circuit measurement results [29]. Fig. 3 showcases the QCAE architecture and the steps involved in image denoising. Given a random Gaussian noise-generating function S, the process involves taking an input data x and subjecting it to the influence of S to produce a noisy input image data version represented as S(x). Subsequently, this noisy input S(x) serves as the input for the QCAE.

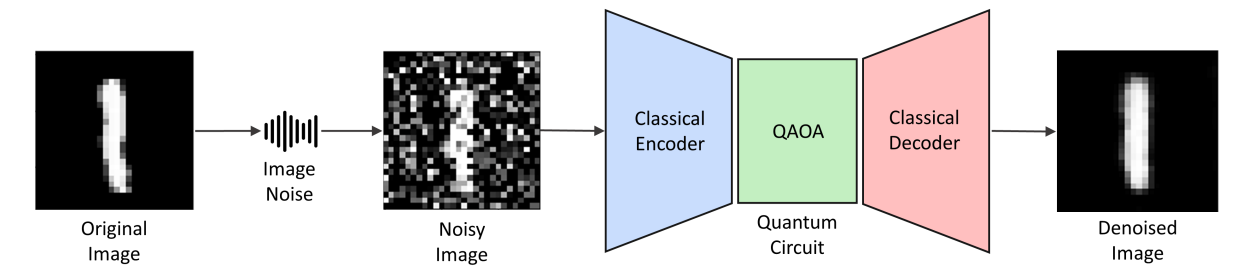


Figure 3: Architecture of quantum convolutional autoencoder, where the classical latent space is replaced with a QAOA circuit to efficiently denoise images.

The training process of the QAOA circuit begins with input image data x and a set of rotation gates at level p. First, the input image is encoded by a classical encoder $\vec{x} = E(x)$, where \vec{x} represents the encoded latent vector [14, 30]. This latent representation is further compressed into a linear form y with dimension 2^p , where $p \ge 1$ corresponds to the QAOA circuit depth. While this step reduces the dimensionality classically, the QAOA circuit operates in a quantum state space of dimension 2^n , with

n denoting the number of qubits, thereby enabling access to richer high-dimensional representations [15, 31]. Classical normalization and optimization methods are then applied to fine-tune the parameters and minimize the cost function. Fig. 5 illustrates this workflow, showing how the classical encoder prepares input data and optimizes it for QAOA circuits at various depths p.

4.2. Quantum approximate optimization algorithm (QAOA)

QAOA, originally proposed by Farhi et al. [32], is a heuristic approach specifically designed to tackle the maxcut problem. It belongs to the group of hybrid algorithms and requires, in addition to executing shallow quantum circuits, a classical optimization process to optimize the parameters and improve the quantum circuit itself [33, 34]. The performance of QAOA continually improves with increasing values of p, where p denotes the number of alternating layers (depth) in the QAOA circuit, which controls the expressiveness of the variational ansatz [35]. As depicted in Fig. 4, the maximum or minimum value of the objective function can be obtained by iteratively finding the optimal values for the parameters γ and β . The iterative process for determining the optimal parameters relies on classical optimization methods. In the context of QCAE, QAOA is adapted to create a quantum latent space representation. latent space aims to generate a compressed encoding of input image data, capturing essential patterns and relationships while reducing dimensionality. The QAOA circuit in QCAE leverages its optimization capabilities to discern quantum information from the input state, creating an optimal latent representation. This approach utilizes QAOA's problem-solving framework to efficiently encode input data in a quantum latent space, potentially offering advantages in data compression and feature extraction for image processing tasks.

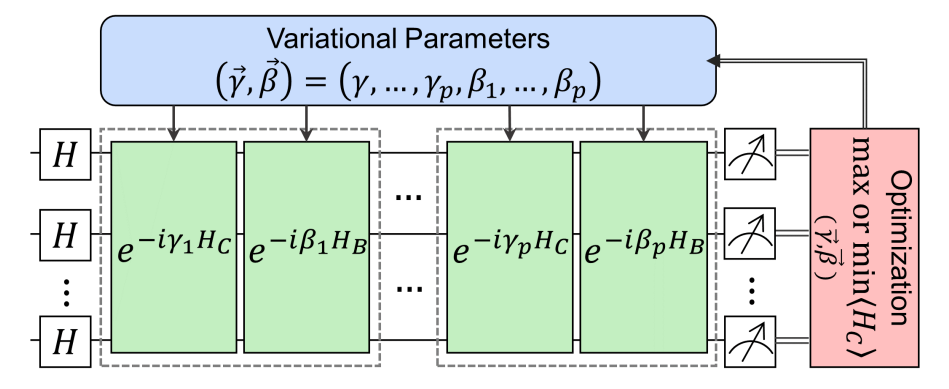


Figure 4: Schematic depicting the quantum approximate optimization algorithm, which integrates a quantum circuit and classical optimization to iteratively optimize variational parameters for enhanced performance.

The algorithm is designed to identify a n-bit binary strings z, the objective function f is defined as follows:

$$f(z): \{0,1\}^n. (10)$$

We can map f to the Hamiltonian H_C as follows:

$$H_C|z\rangle = f(z)|z\rangle.$$
 (11)

In which the phase operators are defined as follows:

$$U_C(\gamma) = e^{-i\gamma H_C},\tag{12}$$

where γ is a parameter. The mixing Hamiltonian H_B is defined as follows:

$$H_B = \sum_{j=1}^n \sigma_j^x,\tag{13}$$

where σ_j^x is the Pauli-X operator. In addition, the mixing operators are defined as follows:

$$U_B(\beta) = e^{-i\beta H_B},\tag{14}$$

where β is a parameter. We can define the state of the p-level QAOA by applying the phase operator and the mixing operator, defined as follows:

$$|\vec{\gamma}, \vec{\beta}\rangle = U_C(\gamma_p)U_B(\beta_p)\cdots U_C(\gamma_1)U_B(\beta_1)|s\rangle,$$
 (15)

with an integer $p \ge 1$ and s is the initial state, defined according to the superposition principle as follows:

$$|s\rangle = |+\rangle^{\otimes n} = \frac{1}{\sqrt{2^n}} \sum_{z} |z\rangle. \tag{16}$$

The expectation value of H_C can be obtained as follows:

$$\langle H_C \rangle := \langle \vec{\gamma}, \vec{\beta} | H_C | \vec{\gamma}, \vec{\beta} \rangle = \langle f \rangle_{(\vec{\gamma}, \vec{\beta})}, \tag{17}$$

where f is the expectation value of the objective function.

Here, we then introduce the process of injecting parameter values into rotation gates R parameter placeholders. The training process of the QAOA circuit begins with input image data x and a set of rotation gates R at level p. First, the input image data are encoded using a classical encoder $\vec{x} = E(x)$, where \vec{x} is an encoded input image data. Then, this data undergoes additional classical processing through convolutional layers, pooling layers, and is transformed into a linear form of y to the size of 2p, where $p \geq 1$ is the QAOA circuit level. While y is classically compressed, the quantum circuit operates on a state space of dimension 2^n , where n is the number of qubits, providing access to high-dimensional quantum representations Classical normalization and optimization techniques are applied to the variable y to fine-tune the parameters, aiming to minimize the objective function (cost function). Fig. 5 illustrates the schematic illustrates the classical encoder in encoding and optimizing input image data for the QAOA circuit at any given p levels.

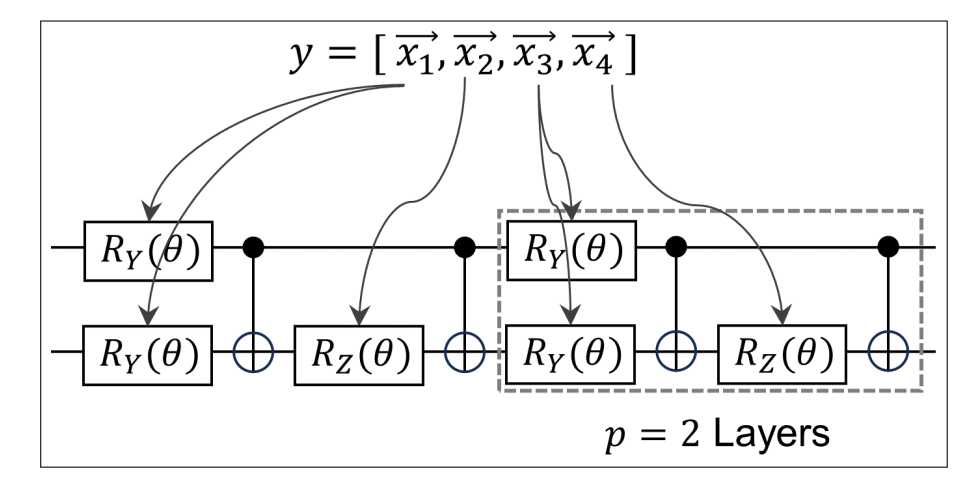


Figure 5: Parameterizing the rotation gates of QAOA circuit with the optimized value of the encoded input image data.

4.3. Parameter-shift rule optimization

In this section, we present a PSR optimization method inspired by [36]. The PSR is a promising approach for evaluating the gradients of QAOA circuits on real quantum machines [37, 38]. Gradients derived from these quantum circuits significantly contribute to the optimization phase of VQAs. In the context of hybrid quantum-classical algorithms, we first construct a quantum circuit and subsequently adjust its parameters to minimize an objective function or cost function [39]. In our proposed method, we compute the gradient of each parameter in the QAOA circuit by per the parameter and determining the difference between two forming a double shift, positive shift and negative shift, on outputs, without modifying the QAOA circuit structure or using any ancilla qubits [36]. Suppose we have an n-qubit QAOA circuit which is parameterized by m parameters, $\theta = [\theta_1, \dots, \theta_i, \dots, \theta_m]$, the objective function $f(\theta)$ of a quantum circuit can be represented by a circuit function as follows:

$$f(\theta) = \langle \psi | U(\theta_i)^{\dagger} Q U(\theta_i) | \psi \rangle, \tag{18}$$

where θ_i is the scalar parameter whose gradient is to be computed and $U(\theta_i)$ is the unitary gate with a parameter θ_i , which is the rotation gate in this paper. For notation simplicity, we will absorb the unitaries before $U(\theta_i)$ into $\langle \psi |$ and $| \psi \rangle$. Unitaries after $U(\theta_i)$ and observables are fused into Q. The parameterized unitary gates can be basically written in the following form:

$$U(\theta_i) = e^{-\frac{i}{2}\theta_i H},\tag{19}$$

where H is the Hermitian generator of $U(\theta_i)$ with only two unique eigenvalues +1 and -1. In this way, the differences in the gradients of the circuit function f with respect

to θ_i are:

$$\frac{\partial f(\theta)}{\partial \theta_i} = \frac{1}{2} (f(\theta_+) - f(\theta_-)),
\theta_+ = [\theta_1, \dots, \theta_i + \frac{\pi}{2}, \dots, \theta_m],
\theta_- = [\theta_1, \dots, \theta_i - \frac{\pi}{2}, \dots, \theta_m],$$
(20)

where θ_+ and θ_- are the positive shift and negative shift of θ , respectively. This method precisely computes the gradient with respect to θ_i , avoiding any approximation errors. We then apply the softmax function to the objective function obtained from measurements $f(\theta)$ as the predicted probability distribution for positive shift and negative shift. Subsequently, we compute the cross entropy between the predicted probability distribution pd and the target distributed td as the classification loss L as follows:

$$L(\theta) = -td^{T} \cdot softmax(f(\theta)) = -\sum_{j=1}^{n} td_{j} \log pd_{j},$$
(21)

where

$$pd_j = \frac{e^{f_j(\theta)}}{\sum_{j=1}^n e^{f_j(\theta)}} \tag{22}$$

Then the gradient of the loss function with respect to θ_i can be defined as follows:

$$\frac{\partial L(\theta)}{\partial \theta_i} = \left(\frac{\partial L(\theta)}{\partial f(\theta)}\right)^T \times \frac{\partial f(\theta)}{\partial \theta_i} \tag{23}$$

Here $\frac{\partial f(\theta)}{\partial \theta_i}$ can be computed on a QAOA circuit utilizing the PSR, while $\frac{\partial L(\theta)}{\partial f(\theta)}$ can be efficiently calculated on classical devices through backpropagation, facilitated by differentiation frameworks, e.g., PyTorch [40] and TensorFlow [41].

Fig. 6 visually depicts the procedural steps of the technique PSR. In each iteration, we perform dual shifts of the parameter θ_i by $+\frac{\pi}{2}$ and $-\frac{\pi}{2}$, respectively. After each parameter shift, we execute the shifted QAOA circuit on either a local quantum simulator or a quantum device. Upon obtaining the results from the two shifted circuits, we apply Equation 20 to calculate the upstream gradient. Following the PSR, we then execute the QAOA circuit without any parameter shift and record the measurement results. Subsequently, we apply softmax and cross-entropy functions to the obtained logits, ultimately producing training loss. The backpropagation process is initiated solely from the loss to the logits, generating downstream gradients. Finally, the gradient is computed by taking the dot product between the upstream and downstream gradients, as outlined in Eq. 23, resulting in the final gradient.

5. Experimental setups

In this section, we outline the datasets used to validate our proposed method and describe the experimental environments for its implementation.

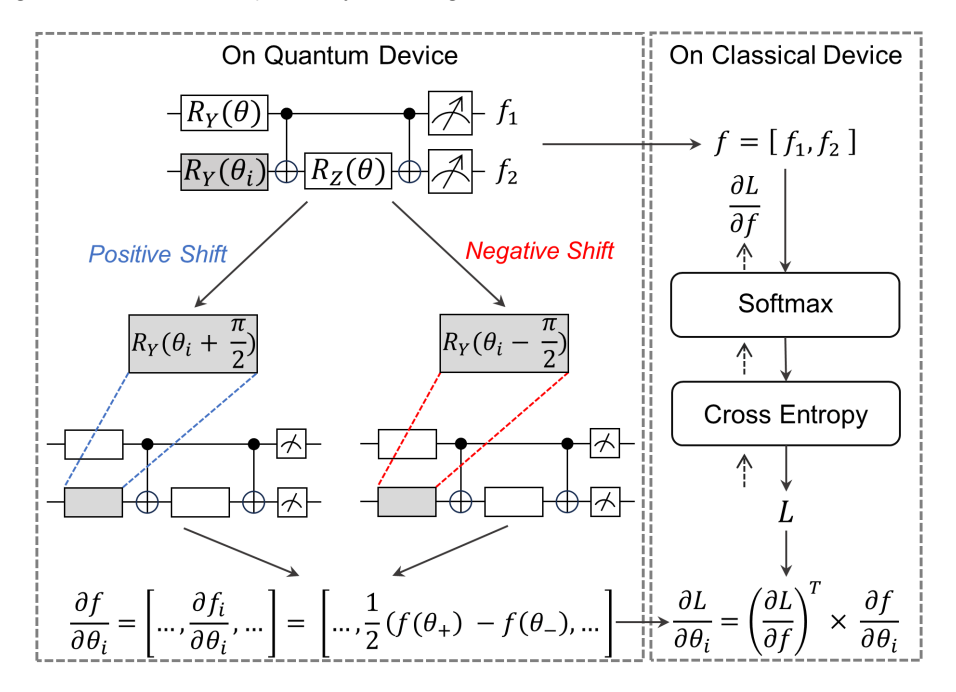


Figure 6: Efficient gradient computation through the technique PSR on a hybrid QAOA circuit.

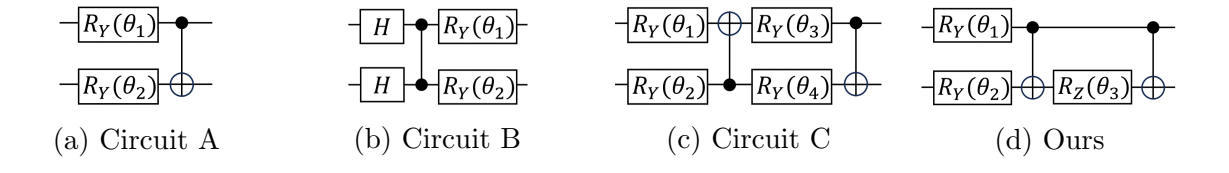


Figure 7: PQCs utilized in the QAOA circuit. The PQCs (a), (b), and (c) are adapted from [31, 42], whereas (d) is our designed QAOA circuit.

5.1. Datasets

We perform both CCAE and QCAE on the well-known MNIST dataset. This dataset comprises handwritten digits presented as grayscale images. The MNIST dataset comprises 60,000 samples in the training set and 10,000 samples in the testing set, each represented by pixels arranged in a shape of $28 \times 28 \times 1$. To incorporate Gaussian noise into the datasets, we used a function that adds random Gaussian noise with standard deviation values $\sigma = \{0.25, 0.5, 0.75, 1\}$ to the images. The original and noisy images are visualized in Fig. 3. Although restricting MNIST to digits 0 and 1 yields 12,000 training and 2,000 test samples, in this study we used smaller subsets to reduce computational cost and accommodate quantum hardware limitations. Specifically, we selected the first 2,000 samples of digits 0 and 1 from the training set (total 4,000 training images) and the first 200 samples of digits 0 and 1 from the test set (total 400 test images). Gaussian noise was applied only to the training set during model optimization, while the test set remained unseen throughout training and was used exclusively for evaluation. This ensures that no overlap occurs between training and testing data. A separate validation

set was not used during training due to the dataset size; model performance was assessed directly on the test set after training. While MNIST is widely used for benchmarking, it has limitations in demonstrating the generalizability and real-world applicability of machine learning models, particularly in the quantum domain, as outlined in [43].

5.2. Environments

The experiments were conducted using the PyTorch [40] and Qiskit [44] frameworks. The proposed QCAE is tested on both a local quantum simulator equipped with a quantum assembly (QASM) simulation and a 27-qubit IBMQ Mumbai quantum machine. For noisy simulators, we leverage the quantum noise model from IBM Mumbai and inject it into the QASM simulator. For notation simplicity, we designate the QASM simulator as the noise simulator, the noisy QASM simulator as the noisy simulator, and the actual quantum machine as the real machine.

For both the CCAE and QCAE, the encoder and decoder architectures comprise three 2D convolutional and 2D transposed convolutional layers, respectively. The only difference lies in the latent space, which is substituted with a QAOA circuit in the case of QCAE. In the CCAE model, the latent space is established through a fully connected layer network, with the classical encoder and decoder employing the LeakyReLU activation function. The training spanned 50 epochs using the Adam optimizer [45] and the mean squared error (MSE) as the loss function. Due to cost and time constraints, we conducted the training in both noiseless and noisy environments, as it required many iterations. To validate the real-world applicability, the testing phase was conducted in a real environment, ensuring the proposed model's reliability in practical scenarios.

We meticulously execute and perform experiments that encompass a comprehensive array of QAOA circuits. These circuits incorporate diverse configurations of single-qubit and two-qubit gate operations. Our circuit designs were inspired by prior research [31, 42], and their visual representation is illustrated in Fig. 7.

6. Experimental results

In this section, we evaluate the performance of our proposed QCAE model on the denoising MNIST dataset. First, we compare the training loss and evaluation of QCAE with CCAE. Second, we analyze the denoising performance of QCAE in *noiseless*, *noisy*, and *real* scenarios. Finally, we conduct ablation studies by varying QAOA circuits and layers to enhance understanding and optimize its overall performance.

6.1. Training of the CCAE and QCAE

In this evaluation, two binary classes were extracted from the MNIST dataset (0 and 1). To gain insights into the distinctions between denoised samples generated by both the CCAE and QCAE models and the original samples, we employ a metric called the

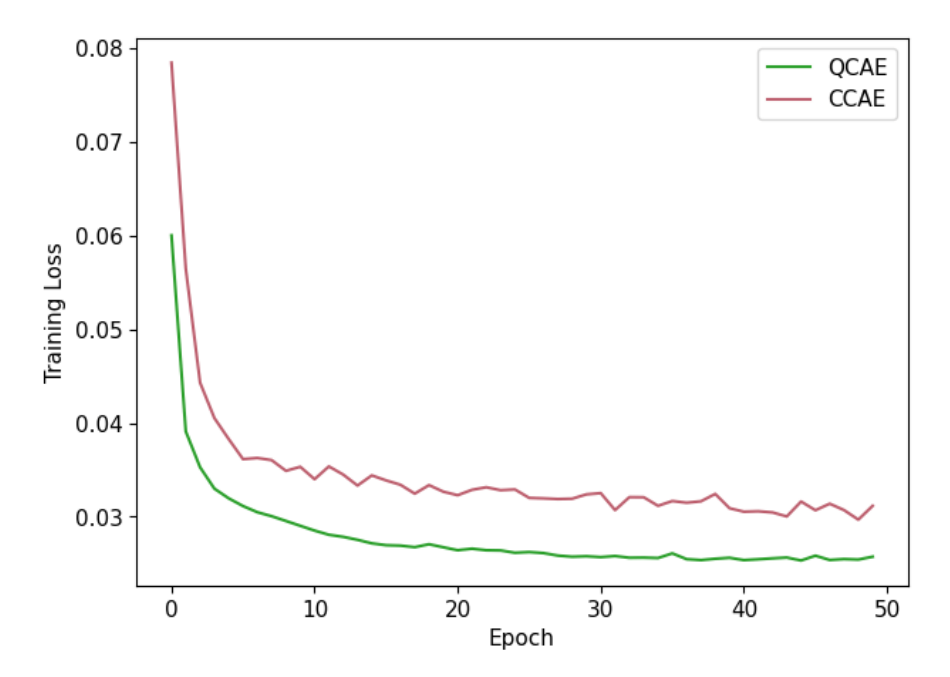


Figure 8: Training loss comparison between CCAE and QCAE over 50 epochs.

structural similarity index measure (SSIM) for analyzing image quality [46], ranging from 0 (worst) to 1 (best). Fig. 8 illustrates the training loss over 50 epochs, where QCAE consistently outperforms CCAE. The corresponding SSIM values are presented in Fig. 10 across all scenarios (*Noiseless, Noisy*, and *Real*). QCAE achieves higher SSIM values than CCAE in most cases. However, at higher noise levels ($\sigma = 0.75$ and 1) in the Real and Noisy scenarios, its SSIM values are slightly lower than those of CCAE, reflecting the impact of quantum hardware noise. Overall, these findings highlight that QCAE consistently delivers robust results when employed for denoising images compared with CCAE.

Fig. 9 depicts original images alongside those with added Gaussian noise, where high corruption levels render them barely visible to the human eye. The denoising results generated using both QCAE and CCAE models are shown alongside the noisy and original images. Notably, in the third row and second column, the CCAE struggles to fully denoise or reconstruct the image, highlighting a limitation. Furthermore, CCAE faces challenges in effectively denoising, resulting in denoised results that exhibit a subtle blurring effect when compared to the sharper outcomes achieved by QCAE, with an average SSIM for CCAE at 0.45 and the SSIM for QCAE at 0.75. This performance gap emphasizes the effectiveness of our proposed QCAE, which outperforms CCAE as its classical counterpart.

6.2. Denoising performance

Here, we conducted denoising of the MNIST images across three distinct scenarios: noiseless, noisy, and real. To effectively demonstrate the performance of the QCAE,

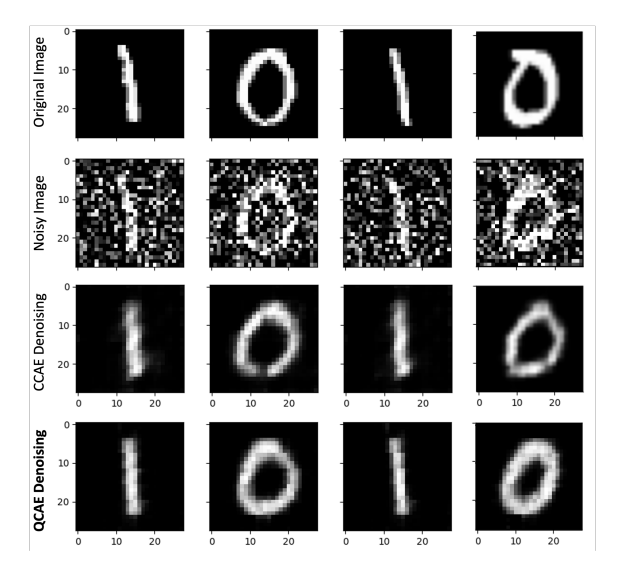


Figure 9: Denoising results on MNIST datasets. The top row displays original images, and the second row shows their noisy counterparts. The third row showcases images denoised with CCAE, and the last row features images denoised using the proposed QCAE method. All images are from the MNIST test set.

we introduced variations in Gaussian noise factors applied to the images because the MNIST does not carry noise. For each scenario, we tested 12 different configurations of Gaussian noise $\sigma = \{0.25, 0.5, 0.75, 1\}$ across three environments (noiseless, noisy, real), and selected the combination that yielded the highest SSIM score for further experiments. The QCAE performance is evaluated for the denoising capability in both quantum simulations and actual machines.

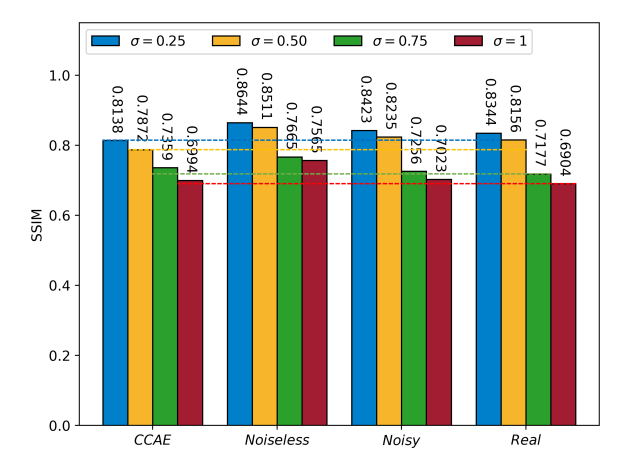


Figure 10: Comparative analysis of the CCAE and specifically QCAE performance under varying conditions, including *noiseless*, *noisy*, and *real* scenarios, with noise factor variations represented by $\sigma = \{0.25, 0.5, 0.75, 1\}$. Evaluation was conducted on the MNIST test set (digits 0 and 1 only).

To analyze the extent of QCAE denoising capabilities, we utilize it to restructure,

denoise, and generate images from a set of Gaussian noisy inputs with varying noise factors values. Even in the presence of high levels of noise, characterized by a noise factor of $\sigma=1$, images that appear indistinguishable to the human eye are effectively processed by QCAE. The algorithm consistently delivers accurate and visually appealing results, demonstrating its robust performance in handling noisy images. Despite testing in noisy and real quantum machine environments, the image maintains readability and closely resembles the original, although with a slight degradation compared to a noiseless environment. As depicted in Fig. 11, denoising results with variations in Gaussian noise levels and quantum machine environments are shown for digit '0' images selected from the same MNIST test subset (digits 0 and 1) used in prior evaluations. This ensures consistency across all noise levels and quantum environments.

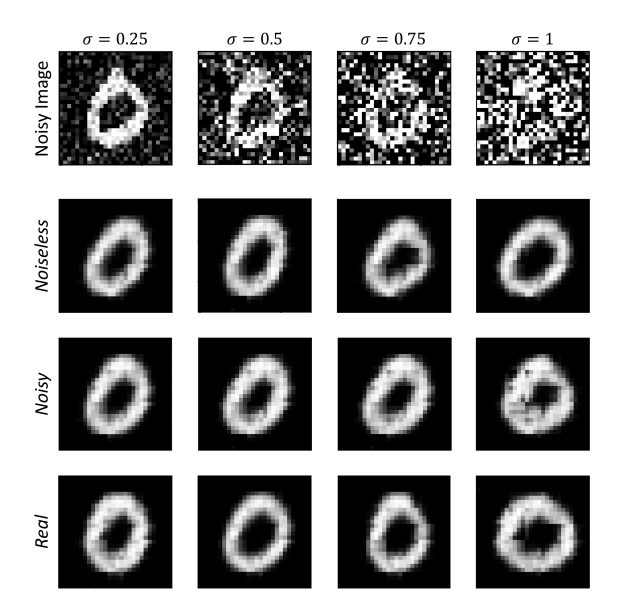


Figure 11: Performance evaluation of QCAE on noisy images across a range of Gaussian noise factors. The top row presents noisy images with $\sigma = \{0.25, 0.5, 0.75, 1\}$. The second row showcases denoised images in a *noiseless* quantum simulation, whereas the third row showcases denoised images in a *noisy* quantum simulation. The fourth row displays denoised images with a *real* quantum machine.

6.3. Comparison of PQCs and PSR optimization

In this study, we conducted experiments employing various quantum circuits sourced from [31, 42], and comparing them to our proposed approach with and without PSR optimization. The experiments were executed with identical configurations, including the number of qubits, epochs, $\sigma=0.5$, optimization using the PSR, a noiseless environment, and the MNIST dataset. In addition, we varied the number of p layers to investigate how circuit depth influences the obtained results. The p-value results were validated across a range from 1 to 5 and subsequently categorized into groups corresponding to the respective quantum circuits. Fig. 12 presents the

SSIM values obtained from the various circuit types depicted in Fig. 7. Compared to alternative circuits, our proposed approach showcases superior performance across these circuits. Specifically, our proposed QAOA circuit consistently outperforms other circuits, showcasing an average improvement of approximately 25% in the SSIM value.

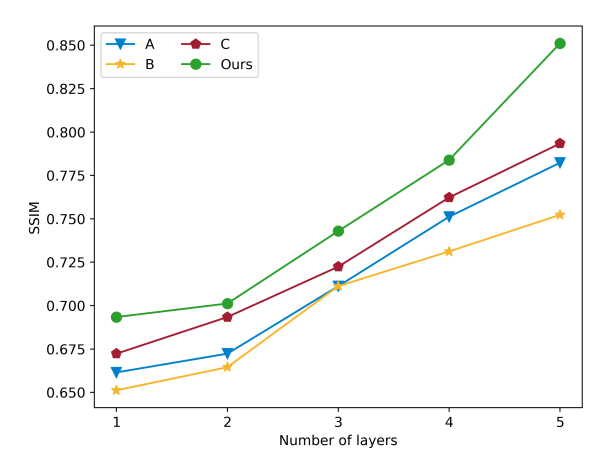


Figure 12: The SSIM value of p ranges from 1 to 5 across all circuits, indicating that better solutions are associated with longer circuit layers. Evaluation was conducted on the same MNIST test subset (digits 0 and 1) used in earlier sections.

We also conducted comprehensive experiments on all circuits, both with and without PSR, resulting in a noteworthy reduction in SSIM values when tested without PSR, as shown in Table 1. Remarkably, our proposed circuit demonstrated the ability to draw comparisons with other circuits, even in the absence of PSR. One plausible explanation is that R_Z gates can be implemented with greater efficiency compared to other single-qubit rotation operations [47]. As we observed, the circuits exhibit lower and significantly higher SSIM values with and without PSR, respectively. This underscores the significance of incorporating PSR optimization to enhance performance. It is noteworthy that the p value significantly influences the results, underscoring its high impact on the outcomes. However, as the parameter p increases, there is a corresponding growth in the circuit execution time. Additionally, our proposed method requires a minimum of two qubits for the efficient denoising of images. It also illustrates the progressive increase in SSIM values corresponding to the varying number of players. As additional layers are added, the QAOA showcases the potential for enhanced approximations towards the optimal solution. Furthermore, it presents the results of experiments conducted on QAOA, both with and without PSR optimization. findings emphasize the significance of employing this optimization technique to identify a lower-cost function, leading to higher accuracy. Through the utilization of the PSR optimization, there is a notable enhancement in SSIM value.

Table 1: The SSIM value for parameter p varies between 1 and 5 across all circuits, both with and without the utilization of PSR optimization techniques.

Circuits	p = 1	p = 2	p = 3	p = 4	p = 5
Without PSR optimization					
A	0.4371	0.4398	0.4423	0.4480	0.4512
В	0.4302	0.4357	0.4423	0.4521	0.4553
\mathbf{C}	0.4493	0.4523	0.4567	0.4623	0.4663
Ours	0.6503	0.6618	0.7034	0.7235	0.7496
With PSR optimization					
A	0.6615	0.6723	0.7112	0.7512	0.7823
В	0.6512	0.6645	0.7112	0.7312	0.7523
\mathbf{C}	0.6723	0.6934	0.7224	0.7623	0.7934
Ours	0.6934	0.7012	0.7429	0.7839	0.8511

7. Conclusion

This study introduced a QCAE model that leverages the power of QAOA to seamlessly substitute for the conventional AE, serving as the latent space. This substitution improves data learning in a higher-dimensional space. We demonstrated the efficiency of our proposed QCAE method through its application to MNIST image denoising. The proposed QCAE method exhibited superior denoising performance, as it achieved lower training loss and increased SSIM, compared to the CCAE method—a finding validated by experimental results—demonstrating its superior capacity to preserve image fidelity. The developed model maintained its superior denoising capabilities when applied to the MNIST dataset. Furthermore, we examined QAOA performance to determine its effectiveness across diverse circuit configurations and layer variations. Finally, we conducted an experiment using PSR optimization to evaluate its impact on QAOA circuit accuracy. This investigation underscores the crucial role of optimization in achieving desirable outcomes. However, we remark that state-of-the-art and out-of-thebox classical algorithms cannot be easily outperformed by current quantum computers and algorithms. Notably, we did not include the mixer QAOA typically used in the QAOA circuits. The reason for this omission is that our primary focus was on evaluating the effectiveness of the QAOA mixing Hamiltonian in enhancing the latent space representation within the QCAE model. In standard QAOA, the mixing Hamiltonian is indeed a fundamental component and is typically chosen as a transverse field. This Hamiltonian helps to explore the solution space by inducing transitions between different quantum states. By isolating the mixing Hamiltonian, we aimed to specially assess its impact on denoising performance without the added complexity introduced by the mixer QAOA. The potential future research directions are as follows: First, we aim to evaluate the effectiveness of our proposed approach by conducting tests on real-world practical

images and providing evidence to validate its viability. Second, we aim to investigate how different optimization methods affect the performance of our proposed model on the MNIST dataset. Furthermore, given that notice noise in real quantum machines can significantly impact the outcomes of the method, employing noise mitigation techniques is required to address and alleviate these effects. Future work will also explore how the dimensionality of the latent space influences the QCAE's representational capacity and learning performance, which could provide insights for optimizing the balance between model complexity and denoising accuracy.

Code available

The code that supports the findings of this study is openly available in the Github repository: Quantum Autoencoder.

CRediT authorship contribution statement

Tara Kit: Conceptualization, Methodology, Validation, Visualization, Software, Writing – review & editing. Kimsay Pov and Kimleang Kea: Writing – review & Validation. Won-Du Chang: Writing – review, Validation, Visualization. Hee Chul Park: Writing – review, Validation. Youngsun Han: Supervision, Validation, Visualization, Writing – review & editing.

Acknowledgments

This research was supported by Quantum Computing based on Quantum Advantage challenge research (RS-2023-00257994) through the National Research Foundation of Korea (NRF) funded by the Korean government (MSIT).

References

- [1] Diwakar M and Kumar M 2018 Biomedical Signal Processing and Control 42 73–88
- [2] Paul E and Sabeenian R 2022 Displays **74** 102258
- [3] Elad M, Kawar B and Vaksman G 2023 SIAM Journal on Imaging Sciences 16 1594–1654
- [4] Izadi S, Sutton D and Hamarneh G 2023 Artificial Intelligence Review **56** 5929–5974
- [5] Wang F, Xu Z, Ni W, Chen J, Pan Z et al. 2022 Computational Intelligence and Neuroscience 2022
- [6] Abiodun O I, Jantan A, Omolara A E, Dada K V, Mohamed N A and Arshad H 2018 *Heliyon* 4
- [7] Sagha H, Cummins N and Schuller B 2017 Wiley Interdisciplinary Reviews: Data Mining and Knowledge Discovery 7 e1212

[8] Leeb F, Bauer S, Besserve M and Scholkopf B 2021 Exploring the latent space of autoencoders with interventional assays Neural Information Processing Systems URL https://api.semanticscholar.org/CorpusID:250113633

- [9] Bouland A, Fefferman B, Landau Z and Liu Y 2022 Noise and the frontier of quantum supremacy 2021 IEEE 62nd Annual Symposium on Foundations of Computer Science (FOCS) (IEEE) pp 1308–1317
- [10] Bharti K, Cervera-Lierta A, Kyaw T H, Haug T, Alperin-Lea S, Anand A, Degroote M, Heimonen H, Kottmann J S, Menke T et al. 2022 Reviews of Modern Physics 94 015004
- [11] Huang H L, Xu X Y, Guo C, Tian G, Wei S J, Sun X, Bao W S and Long G L 2023 Science China Physics, Mechanics & Astronomy 66 250302
- [12] Lecun Y, Bottou L, Bengio Y and Haffner P 1998 Proceedings of the IEEE 86 2278–2324
- [13] Schneider S, Antensteiner D, Soukup D and Scheutz M 2022 Autoencodersa comparative analysis in the realm of anomaly detection *Proceedings of the IEEE/CVF Conference on Computer Vision and Pattern Recognition* pp 1986– 1992
- [14] Bravo-Prieto C 2021 Machine Learning: Science and Technology 2 035028
- [15] Rivas P, Zhao L and Orduz J 2021 Hybrid quantum variational autoencoders for representation learning 2021 International Conference on Computational Science and Computational Intelligence (CSCI) (IEEE) pp 52–57
- [16] Orduz J, Rivas P and Baker E 2021 Transactions on Computational Science and Computational Intelligence. Springer
- [17] Nguyen N T and Kenyon G T 2018 Image classification using quantum inference on the d-wave 2x 2018 IEEE International Conference on Rebooting Computing (ICRC) (IEEE) pp 1–7
- [18] Sleeman J, Dorband J and Halem M 2020 A hybrid quantum enabled rbm advantage: convolutional autoencoders for quantum image compression and generative learning *Quantum information science*, sensing, and computation XII vol 11391 (SPIE) pp 23–38
- [19] National Academies of Sciences E, Medicine et al. 2019
- [20] Nielsen M A and Chuang I L 2010 Quantum computation and quantum information (Cambridge university press)
- [21] Stein S A, L'Abbate R, Mu W, Liu Y, Baheri B, Mao Y, Qiang G, Li A and Fang B 2021 A hybrid system for learning classical data in quantum states 2021 IEEE International Performance, Computing, and Communications Conference (IPCCC) (IEEE) pp 1–7
- [22] Cortese J A and Braje T M 2018 arXiv preprint arXiv:1803.01958
- [23] Wang Y, Wang Y, Chen C, Jiang R and Huang W 2022 Neurocomputing **501** 566–582

[24] Ovalle-Magallanes E, Alvarado-Carrillo D E, Avina-Cervantes J G, Cruz-Aceves I and Ruiz-Pinales J 2023 Applied Soft Computing 141 110307

- [25] Benedetti M, Lloyd E, Sack S and Fiorentini M 2019 Quantum Science and Technology 4 043001
- [26] Hubregtsen T, Pichlmeier J, Stecher P and Bertels K 2021 Quantum Machine Intelligence 3 1–19
- [27] Baldi P 2012 Autoencoders, unsupervised learning, and deep architectures Proceedings of ICML workshop on unsupervised and transfer learning (JMLR Workshop and Conference Proceedings) pp 37–49
- [28] Yan S, Shao H, Xiao Y, Liu B and Wan J 2023 Robotics and Computer-Integrated Manufacturing 79 102441
- [29] Hassan E, Hossain M S, Saber A, Elmougy S, Ghoneim A and Muhammad G 2024 Biomedical Signal Processing and Control 87 105560
- [30] Shiba K, Sakamoto K, Yamaguchi K, Malla D B and Sogabe T 2019 arXiv preprint arXiv:1906.01196
- [31] Kim J, Huh J and Park D K 2023 Neurocomputing 555 126643
- [32] Farhi E, Goldstone J and Gutmann S 2014 arXiv preprint arXiv:1411.4028
- [33] Guerreschi G G and Matsuura A Y 2019 Scientific reports 9 6903
- [34] Choi J and Kim J 2019 A tutorial on quantum approximate optimization algorithm (qaoa): Fundamentals and applications 2019 International Conference on Information and Communication Technology Convergence (ICTC) (IEEE) pp 138–142
- [35] Farhi E and Harrow A W 2016 arXiv preprint arXiv:1602.07674
- [36] Wang H, Li Z, Gu J, Ding Y, Pan D Z and Han S 2022 Qoc: quantum onchip training with parameter shift and gradient pruning *Proceedings of the 59th* $ACM/IEEE\ Design\ Automation\ Conference\ pp\ 655-660$
- [37] Crooks G E 2019 arXiv preprint arXiv:1905.13311
- [38] Wierichs D, Izaac J, Wang C and Lin C Y Y 2022 $\mathit{Quantum}~\mathbf{6}$ 677 ISSN 2521-327X
- [39] Romero J, Olson J P and Aspuru-Guzik A 2017 Quantum Science and Technology 2 045001
- [40] Paszke A, Gross S, Massa F, Lerer A, Bradbury J, Chanan G, Killeen T, Lin Z, Gimelshein N, Antiga L et al. 2019 Advances in neural information processing systems 32
- [41] Abadi M, Agarwal A, Barham P, Brevdo E, Chen Z, Citro C, Corrado G S, Davis A, Dean J, Devin M et al. 2016 arXiv preprint arXiv:1603.04467
- [42] Hur T, Kim L and Park D K 2022 Quantum Machine Intelligence 4 3
- [43] Bowles J E, Ahmed S and Schuld M 2024 arXiv (Preprint 2403.07059)
- [44] Qiskit contributors 2023 Qiskit: An open-source framework for quantum computing

- [45] Kingma D P and Ba J 2014 arXiv preprint arXiv:1412.6980
- [46] Tanchenko A 2014 Journal of Visual Communication and Image Representation 25 874–878

 $[47]\,$ McKay D C, Wood C J, Sheldon S, Chow J M and Gambetta J M 2017 Physical Review A ${\bf 96}\ 022330$